Contents

4 Photon Beam **2**

4.1 Choice of technique 3

4.1.1 Compton back-scatter 4

4.1.2 Tagged bremsstrahlung 6

4.1.3 Coherent bremsstrahlung 7

4.2 Photon Source 9

4.2.1 Essential features 11

4.2.2 Use of collimation 12

4.2.3 Choice of radiator 18

4.2.4 Crystal thickness 21

4.2.5 Crystal mount 22

4.2.6 Crystal quality and lifetime 24

4.3 Electron Beam 25

4.3.1 Beam emittance requirements 26

4.3.2 Electron beam line optics 29

4.3.3 Electron beam dump 30

4.4 Tagging Spectrometer 30

4.4.1 Magnet 30

4.4.2 Spectrometer Optics 32

4.4.3 Focal-plane hodoscope 32

4.5 Operating Beam Intensity 35

Chapter 4

Photon Beam

One of the unique opportunities presented by a CEBAF upgrade to energies of 8 GeV and beyond is the possibility of generating high-intensity c.w. photon beams for high energy photoproduction experiments. In this regime, photon beams represent an interesting extension to the meson spectroscopy program that has been actively pursued using beams of pseudoscalar mesons at hadron accelerator laboratories: with high energy photons one has essentially a beam of *vector* mesons. It is difficult, in fact, to conceive of any other way to obtain such a vector beam.

The requirements for photon beam energy and polarization were described in chapter 3. This chapter describes a design for a real photon facility that meets these requirements. Starting with a beam of monochromatic electrons, it provides an intense beam of high-energy photons with an energy spectrum that is dominated by a single peak. Nearly half of the total power in the beam is concentrated inside this peak, which has a width of less than 10% f.w.h.m. At a fixed electron beam energy E_0, the peak energy of the photon beam can be varied anywhere from below 50% up to 90% E_0 simply by rotating a crystal. The photon spectrum inside the intensity peak has a large degree of plane polarization. The precise energy of an individual photon inside the peak is determined ("tagged") from the momentum of the recoil electron measured in a dedicated "tagging" spectrometer. The design is formed around the expected parameters for the CEBAF beam following the energy upgrade to 12 GeV, although nothing prevents its operation at lower energies before the time that 12 GeV beams are available. The design of the tagging spectrometer makes allowance for operation at energies up to 20 GeV, in the event of a further energy upgrade in the future.

This chapter begins with a survey of the techniques for producing high-energy photons that were considered in the development of this design, and

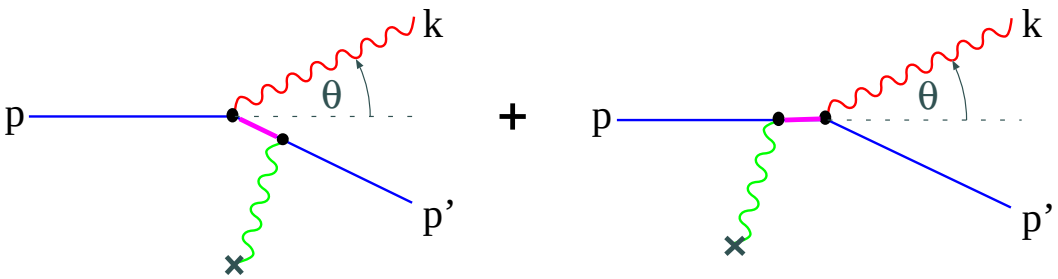

Figure 4.1: Generic diagrams for hard photon production from a high energy electron beam. The symbol $\times$ represents either a static charge distribution, in the case of virtual photons in the initial state (i.e. bremsstrahlung), or an optical cavity, in the case of real photons in the initial state (i.e. Compton scattering).

the reasons for the choice of coherent bremsstrahlung. The coherent bremsstrahlung source is then described in greater detail, followed by a discussion of the requirements that the design places on the electron beam that feeds the source. The tagging spectrometer design is described next, and the chapter concludes with a discussion of the considerations that govern the choice of beam intensity for particular measurements.

4.1 Choice of technique

Two basic methods have been considered for producing photons of the highest possible energy, flux and polarization from electrons of 12 GeV. The methods are bremsstrahlung and Compton scattering of light. Both are well-established methods of producing photon beams. Both techniques are actually described by the same Feynman diagrams, shown in Fig. 4.1. In the case of Compton scattering the incoming photon is real, whereas it is virtual for the case of bremsstrahlung.

Each of these techniques has its own limitations and advantages. In order to be suitable for HALL D, the photon source must be capable of producing photons of energy at least 80% E_0. The photon beam should have linear polarization. The energy resolution for individual photons in the beam should be as good as possible, *i.e.* on the order of the energy spread of the electron beam itself. It should be capable of producing fluxes up to 10^8/s. The contamination of the beam with photons outside the desired energy band should be as low as possible. It is also important that the source should be reliable and require a minimum of down-time for maintenance. The suitability of each

approach is discussed below in the light of these criteria.

4.1.1 Compton back-scatter

A Compton source begins with a beam of visible or ultraviolet light, typically from a laser, that is aligned to intersect the incident electron beam at close to 180°. Some of the photons undergo Compton scattering with the beam electrons. In the lab frame, the scattered photons come out in a narrow cone about the incident electron direction, and carry a significant fraction of the electron energy.

The basic design of the Compton back-scatter source for this study was put forward by from C. Keppel and R. Ent [1]. The design entails the use of a four-mirror high-gain cavity pumped by a 10kW argon-ion laser putting out $2\,ps$ pulses at a frequency of 100 MHz. The pulses in the cavity are synchronized so that the light pulses intercept an electron bucket each time they pass through the beam. The total length of the cavity is $2\,m$ with a crossing angle of 1°. Both cavity and electron beam are focused to a tiny spot of 10 μm r.m.s. radius at the crossing point. A small spot size is necessary in order to get as high a scattering rate as possible. The gain of the cavity is 10^4, which is conservative in view of recent advances in mirror technology. The wavelength of the light is $514\,nm$. The rate spectrum of the back-scattered beam from this source is shown in Fig 4.2a for a 1μA electron beam at 12 GeV.

From the point of view of flux, this source is marginal. With a few μA of beam and mirror improvements, it might produce 10^8 photons/s in the upper 1/3 of its energy spectrum. However, its maximum photon energy of 3.7 GeV is far short of the 80% E_0 needed for HALL D. To remedy this one must decrease the wavelength of the laser beam. This can be done by the use of a frequency-doubling crystal that absorbs the green light from the laser and produces ultraviolet light at $257\,nm$. Storing this light in a cavity of similar design to that described above yields the back-scatter rate spectrum shown in Fig. 4.2b. The major reason for the drop in rate is the decrease in the cavity gain from 10000 to 250. This is imposed by the diminished reflectivities of mirrors in the UV. Other factors are the inefficiency of the doubling crystal, a factor of two in rate from the doubling itself, and the decreasing Compton cross section with energy. The maximum photon energy is still under 50% E_0 and the flux is three orders of magnitude below the desired rate.

In order to reach photon energies of 80% E_0, initial photons of $20eV$ are needed. The brightest sources of these would be a synchrotron light source or a free electron laser (FEL). Mirrors that operate at these wavelengths typically have reflectivities around 70%. With these one could conceive of a scheme that

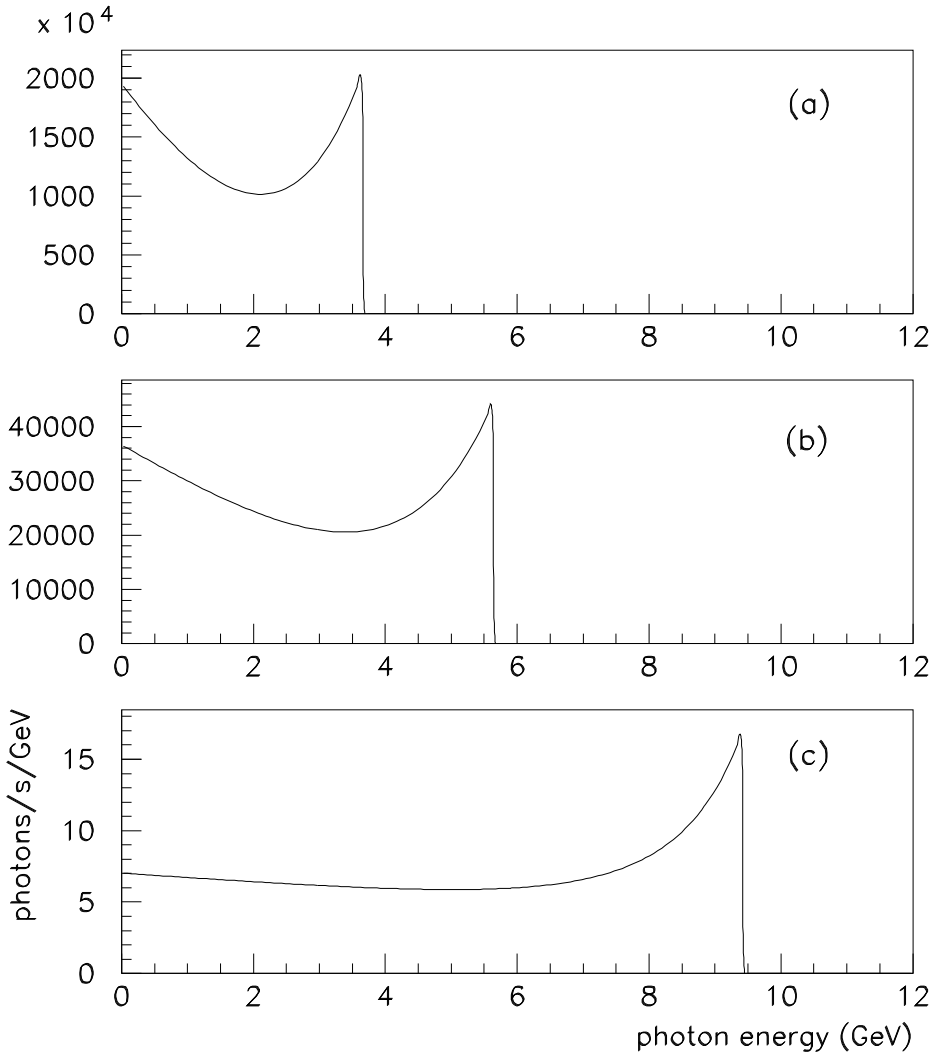

Figure 4.2: Photon energy spectrum from the Compton back-scatter source described in the text and a 12 GeV electron beam at 1μA. (a) cavity of gain 10000 driven by a 10kW Argon-ion laser (514 nm) pulsed at 100 MHz. (b) cavity of gain 250 driven by 3kW frequency-doubler (257nm) pulsed at 100 MHz. (c) cavity of gain 1 driven by a hypothetical FEL source operating at 20eV with same structure as CEBAF beam, peak power 1kW.

uses a wiggler to extract energy from the 12 GeV beam before it enters the dump. This light would have the same time structure as incident beam, and so it could be reflected back and made to cross the incident beam at a small angle, for a Compton back-scatter source. An indication of the level of flux that could be achieved with such a source can be obtained by using the laser cavity model described above, setting the gain to 1, the wavelength to 62 nm, and assuming 1kW peak (1W average) of synchrotron light. The back-scatter rate is shown in Fig 4.2c. This plot shows that even if the full power of a 1μA 12 GeV beam were converted into 20eV photons and backscattered from the incoming beam, the rate would still fall far short of the requirements for HALL D.

From the point of view of polarization, the Compton back-scatter source would be ideal. The polarization of the back-scattered beam is controlled by that of the laser, and can be essentially 100%. This source is also virtually background-free because the spectrum below any desired cutoff can be eliminated by collimation. The energy of the remaining beam can be measured to within the resolution of the electron beam by tagging. However the the combination of sufficient energy and sufficient flux for the purposes of HALL D cannot be achieved using this source.

4.1.2 Tagged bremsstrahlung

A bremsstrahlung source consists of a thin piece of material (the radiator) that is placed in the electron beam and converts part of the energy of the beam into bremsstrahlung radiation. Bremsstrahlung offers the only practical way, starting with an electron beam at CEBAF energies, to produce a photon beam with a significant flux in the vicinity of the end point. It produces a naturally collimated photon beam with a characteristic angular spread of m/E_0. This allows the low emittance of the CEBAF beam to be effectively transfered into the secondary photon beam.

Bremsstrahlung does not suffer from the kind of flux limitations that were encountered in the examination of Compton back-scatter sources. The radiator thickness must be kept below 1% of a radiation length in order to maintain good energy resolution in the tagger. Keeping the thickness below 10^{-3} radiation lengths ensures that multiple scattering in the radiator does not significantly broaden the divergence angle of the photon beam. A 10^{-3} radiator and 1μA of electrons would produce much more than sufficient flux for HALL D.

A bremsstrahlung source is, however, deficient in some other respects. Averaged over the bremsstrahlung cone, the photon beam has zero plane polar-

ization. Circular polarization can be achieved by polarization transfer from a circularly polarized electron beam, but for the purposes of HALL D it is plane polarization that is desired. A bremsstrahlung source also suffers from a large low-energy flux in the beam. The power spectrum of a bremsstrahlung beam is approximately uniform from zero up to the energy of the incident electrons. This means that an experiment that uses the high-energy part of the beam must operate in a background of low-energy photons that are many times more frequent. The tagger is helpful in eliminating many of the false starts in the detector that arise from the background, but this technique becomes ineffective at rates above a few 10^7 tagged photons/s. For the typical experiment using tagged bremsstrahlung and open detector geometry, background from low-energy beam particles limits the rate at which the experiment can run to less than $5 \cdot 10^7$ tagged photons/s. The goal for HALL D pushes that limit to 10^8/s.

4.1.3 Coherent bremsstrahlung

The source described in the previous section meets most of the requirements for HALL D, but is deficient in the areas of polarization and backgrounds. Both of these deficiencies can be remedied by replacing the conventional amorphous or polycrystalline radiator with a thin mono-crystalline wafer. At special settings for the orientation of the crystal, the atoms in the radiator can be made to recoil together from the radiating electron. When they do this they produce a coherent enhancement at particular energies in the radiation spectrum, which correspond to the reciprocal lattice vectors of the crystal. The kinematics are such that a randomly oriented lattice vector would make a tiny peak located up at the end point of the energy spectrum, where the coherent gain factor is negligible. By careful orientation of the crystal, however, one of the lattice vectors can be aligned with the favored kinematics for bremsstrahlung, at which point its coherent peak appears well below the end point, and its coherent gain can be large enough that it contributes a large fraction of the total radiated power.

This is illustrated in Fig. 4.3. This plot shows the intensity (EdN/dE) or power spectrum of the coherent bremsstrahlung beam after collimation. The sequence of secondary peaks above the primary correspond to integral multiples of the primary reciprocal lattice vector and so they are always present. By careful choice of orientation angles it is possible to suppress all other vectors and isolate just one primary peak. By rotating the crystal, the position of the peak can be moved from one end of the spectrum to the other. Note that the coherent peaks appear on top of the incoherent bremsstrahlung continuum.

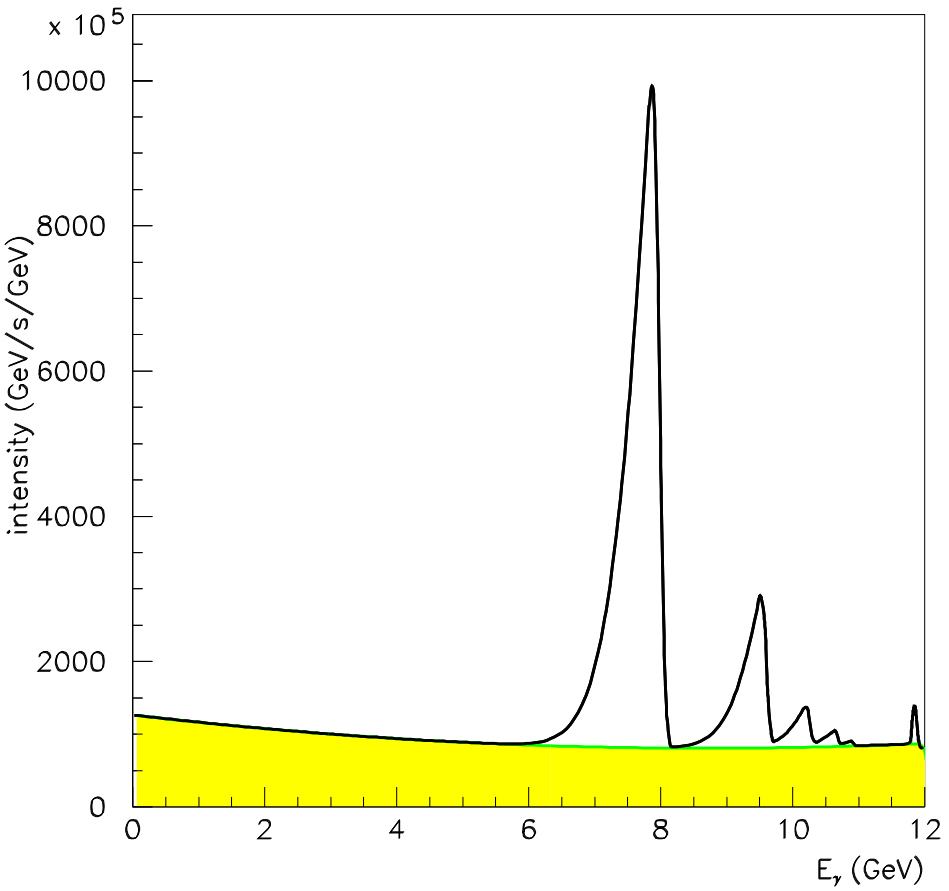

Figure 4.3: Photon power spectrum from an oriented diamond radiator. The y axis is dP/dE with power P expressed in GeV/s and E in GeV. The radiator thickness is 10^{-4} radiation lengths and the electron beam current is 1μA. Shown is what emerges after the photon beam passes through a collimator $3.4\,mm$ in diameter located $80\,m$ downstream from the radiator.

Unlike the underlying continuum, the photons in the coherent peak have significant net linear polarization in the plane given by the beam direction and the crystal lattice vector. This polarization is enhanced by collimating the photon beam beyond its intrinsic angular spread, as discussed in the next section. The loss in flux from collimation can be recovered by increasing the crystal thickness or the electron beam current. As will be shown in the following section, even in the case of very thin crystals and severe collimation, only modest electron beam currents are needed to produce the required photon flux.

The use of coherent bremsstrahlung improves the background conditions by increasing the ratio of hard to soft photons in the beam. For measurements that do not require polarization, a crystal radiator can be used without collimation to reduce the amount of low-energy background for a given rate of tagged photons. Where polarization is required, coherent bremsstrahlung is indispensable.

4.2 Photon Source

A horizontal plan view of the photon beam line is shown in Fig. 4.4 with the major components labeled. The electron beam enters the figure from below ground at the left and is bent into the horizontal plane to enter the tagger building. There it passes through two small dipoles to impinge upon the bremsstrahlung radiator. After its exit from the radiator, the electron beam passes into the tagger magnet where the primary beam is bent in the direction of the electron beam dump. The radiator crystal is thin enough that most of the electrons lose less energy in traversing the radiator than the intrinsic energy spread of the incident beam. Those electrons which lose a significant fraction of their initial energy inside the radiator do so by emitting a single bremsstrahlung photon. These degraded electrons are bent out of the primary beam inside the tagger magnet and exit the vacuum through a thin window, passing through air for a short distance to strike the focal plane of the spectrometer. The primary electron beam is contained inside vacuum all the way to the dump. The two dipole magnets shown in the figure downstream of the tagger may not be necessary if the deflection angle of the primary beam inside the tagger magnet is deemed to be sufficient.

The photons that are produced in the radiator pass through a small hole bored in the return yoke of the tagger magnet to exit the vacuum through a thin window in the forward direction. They then pass into a transfer pipe, which may either be evacuated or filled with helium to reduce photon beam

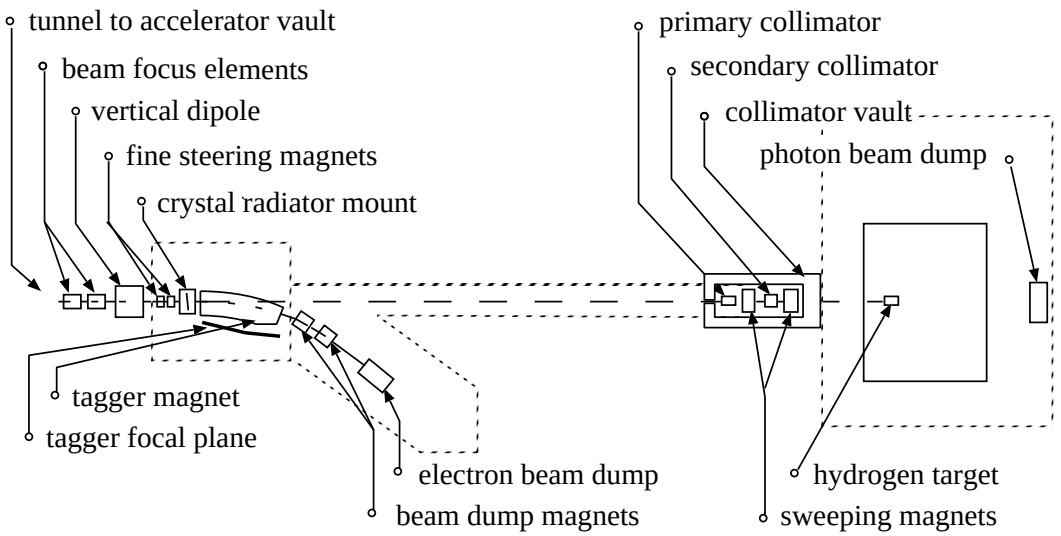

Figure 4.4: Schematic plan view of the photon beam line, shown in the horizontal plane as viewed from above. The objects in this figure are not drawn to scale.

degradation due to interactions, and travel to the experimental hall. Just before entering the hall the photon beam passes through a system of collimators and sweeping magnets. In the figure they are shown in a separate enclosure for shielding purposes. The primary collimator is first. It defines the part of the photon beam that is allowed to reach the target. Debris from interactions along the inside surface of the collimator bore forms a halo around the photon beam that exits the collimator. The charged component of the halo is deflected away from the beam axis by a dipole "sweeping" magnet just downstream of the collimator. A secondary collimator follows the sweeping magnet to stop the deflected shower particles and block the halo of secondary photons generated by the first collimator. The secondary collimator is of a larger diameter than the primary and so sees a reduced rate of secondary interactions on the inner surface of the hole. What new showers are generated there are cleaned up by a second sweeping magnet. The beam then passes through a final collimating aperture into the experimental hall. This triple-collimation system was copied from the setup developed at SLAC [2].

The collimated photon beam, now only a few *mm* in diameter, is delivered to the experimental target. After passing through of order 3% radiation lengths of target, the photon beam passes through the detector and into the photon beam dump at the back of the hall. Based upon a design upper limit of 60kW

(5μA at 12 GeV) being delivered to the electron beam dump, the total power in the photon beam is at most 1.5W in the experimental hall and at most 15W in the collimator enclosure.

4.2.1 Essential features

The adjective 'coherent' in coherent bremsstrahlung does not indicate that the photons in the beam are in a coherent state, as is light from a laser. Rather it refers to the coherent effect of multiple atoms in a crystal lattice in absorbing the recoil momentum from a high energy electron when it radiates a bremsstrahlung photon. In X-ray spectroscopy one encounters the same thing in the Mössbauer effect, except in that case the chief physical consequence is the disappearance of the recoil Doppler shift from the photoabsorption/emission spectrum. Here the chief consequence is the enhancement of bremsstrahlung at those particular kinematics for which the recoil momentum matches one of the reciprocal lattice vectors of the crystal.

Another useful way to view the process of coherent bremsstrahlung is as virtual Compton scattering. To the high energy electron, the atoms in the radiator appear as clouds of virtual photons. For a disoriented radiator material, the virtual photon spectrum is given simply by the atomic form factor, averaged over the different species in the material. If the radiator is a single crystal, however, the atomic form factor gets multiplied by the form factor of the crystal, which in the ideal case looks like a series of delta-functions located at the sites of the reciprocal lattice. In effect, the crystal provides a set of virtual laser beams, each one a standing wave tuned to a specific reciprocal lattice vector. In this view the process of hard bremsstrahlung is seen to be the same as Compton back-scattering of laser light. For a more detailed discussion of the physics of coherent bremsstrahlung there are a number of good references [2, 3, 4, 5].

The use of Compton back-scattering of laser light as a photon source was earlier noted as ruled out by the limitation of high-power lasers and cavities to wavelengths above 100 μm. The characteristic wavelength of the crystal photons is a few Angstroms, three orders of magnitude shorter. In this case, 180° scattering would result in essentially 100% of the electron beam momentum being transfered to the photon in the lab frame. However, the Compton cross section contains a factor of $1/(\vec{q} \cdot \vec{p})^2$ where $\vec{q}$ is the virtual photon momentum and $\vec{p}$ is that of the electron, which strongly favors incident photons with $\vec{q}$ nearly orthogonal to $\vec{p}$. With reciprocal lattice vectors pointing in almost every direction, only those nearly perpendicular to the beam contribute appreciably to the scattering rate. This fact applies equally to ordinary brems-

strahlung; in fact, to a first approximation the bremsstrahlung spectrum from a single crystal is the same as from a disoriented radiator. The reason is that, if the sum over crystal momenta were replaced with a continuous integral, one would recover the ordinary bremsstrahlung result for isolated atoms. Beyond a few unit cells from the origin in reciprocal lattice space, the atomic form factor and kinematic factors become slowly varying on the scale of the lattice spacing, and the sum becomes indistinguishable from the integral. Besides that, the uncertainty principle requires that atoms localized at the sites in a crystal undergo fluctuations about their mean position. This has the effect of attenuating the discrete peaks in the crystal form factor at progressively higher-order crystal momenta, eventually washing them out and filling in the gaps between them, so that the sum deforms smoothly into the integral at high momentum transfer. Hence, the sum over crystal indices that yields the final photon spectrum can be separated into two parts: a discrete sum over a limited set of small crystal indices and an integral over the continuum of momentum transfer values beyond. The latter appears in the coherent bremsstrahlung beam as an ordinary $1/k$ bremsstrahlung spectrum, while the former appears as a set of peak structures superimposed upon it. The $1/k$ continuum, referred to as the incoherent component, is invariant as the crystal is rotated, whereas the coherent peaks change in position and intensity, depending on crystal orientation.

A typical coherent bremsstrahlung spectrum is shown in Fig. 4.5. The distinction between incoherent and coherent components in the figure is artificial; it is there to show the part of the spectrum that shifts as the crystal is rotated. The vertical scale in the figure gives the photon rate for the given beam current and crystal thickness. Note that the intensity of the incoherent background is less than what would be obtained with an amorphous carbon radiator of the same thickness, because a part of the momentum transfer integral in the Bethe-Heitler formula has been moved into the discrete sum and contributes to the coherent part. The radiation length of diamond is actually an average over all orientations of the crystal. In the calculation for Fig. 4.5 the leading 400 lattice sites were included in the discrete part of the calculation, although it can be seen that only two or three of them contribute with sufficient intensity to be individually visible in the spectrum.

4.2.2 Use of collimation

The presence of the large incoherent flux in Fig. 4.5 presents a significant handicap to a photoproduction experiment. Not only do the low energy photons produce background in the detector, but they diminish the polarization of the

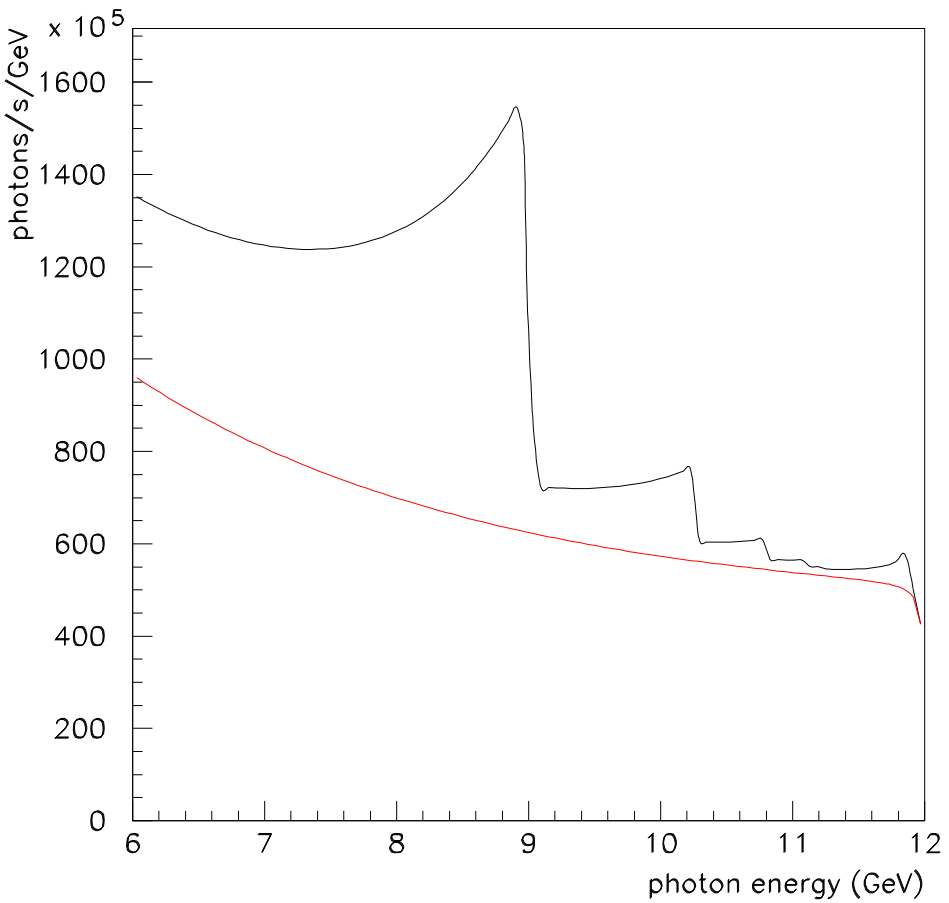

Figure 4.5: Coherent bremsstrahlung spectrum, calculated for a diamond crystal radiator 15μm thick and a 1μA electron beam of 12 GeV energy. Typical values were used for beam emittance and crystal mosaic spread.

beam. The entire beam polarization appears in the coherent component; the underlying incoherent flux only serves to dilute the polarization. There is another difference between the two components that allows them to be separated to some extent. The kinematics of bremsstrahlung confines most of the intensity of the photon beam to forward angles within m/E radians of the incident electron direction. In the lab this is a small angle, but in the rest frame of the electron-photon system it subtends all angles in the forward hemisphere. A peak in the coherent component that corresponds to a single reciprocal lattice vector has two-body kinematics, so there is a well-defined relation between the emission angle and the energy of the emitted photon in the lab: emission at 0° yields a maximum energy photon, with energy decreasing with increasing angle. This accounts for the shape of the coherent peaks in Fig. 4.5, with the sharp right-hand edge corresponding to 0° emission and the tail to lower energies corresponding to scattering into higher angles.

The incoherent component, because it comes from a sum over momentum transfers at all angles, has essentially no correlation between photon energy and emission angle. This means that collimating away all photons beyond some angle $\theta_{max} < m/E$ uniformly attenuates the incoherent spectrum at all energies, whereas it preserves all of the coherent photons from the maximum energy for the given peak down to some cutoff. The kinematic relations for coherent bremsstrahlung are as follows,

$$\theta^2 + 1 = \left(\frac{1-x}{x}\right)\left(\frac{x_{max}}{1-x_{max}}\right) \tag{4.1}$$

$$x_{max} = \frac{2\vec{p}\cdot\vec{q}}{2\vec{p}\cdot\vec{q} - m_e^2} \tag{4.2}$$

where x is the photon energy in units of the incident electron energy and θ is the lab emission angle of the photon relative to the incident electron momentum axis, in units of m/E .

The effects of collimation are demonstrated in the calculated spectra shown in Fig. 4.6. First, note that the collimation angles are very small, which requires a long flight path of order $100\,m$ in order that the collimator can be larger than the intrinsic beam spot size, otherwise the collimator is cutting in transverse coordinate instead of in angle. This distance is, in fact, a sensitive function of the electron beam emittance from the machine, and must be increased in inverse proportion to the beam emittance if the effectiveness of collimation is to be maintained. This issue, along with the associated demands placed on beam alignment and position stability, are taken up in more detail in the following section on the electron beam line.

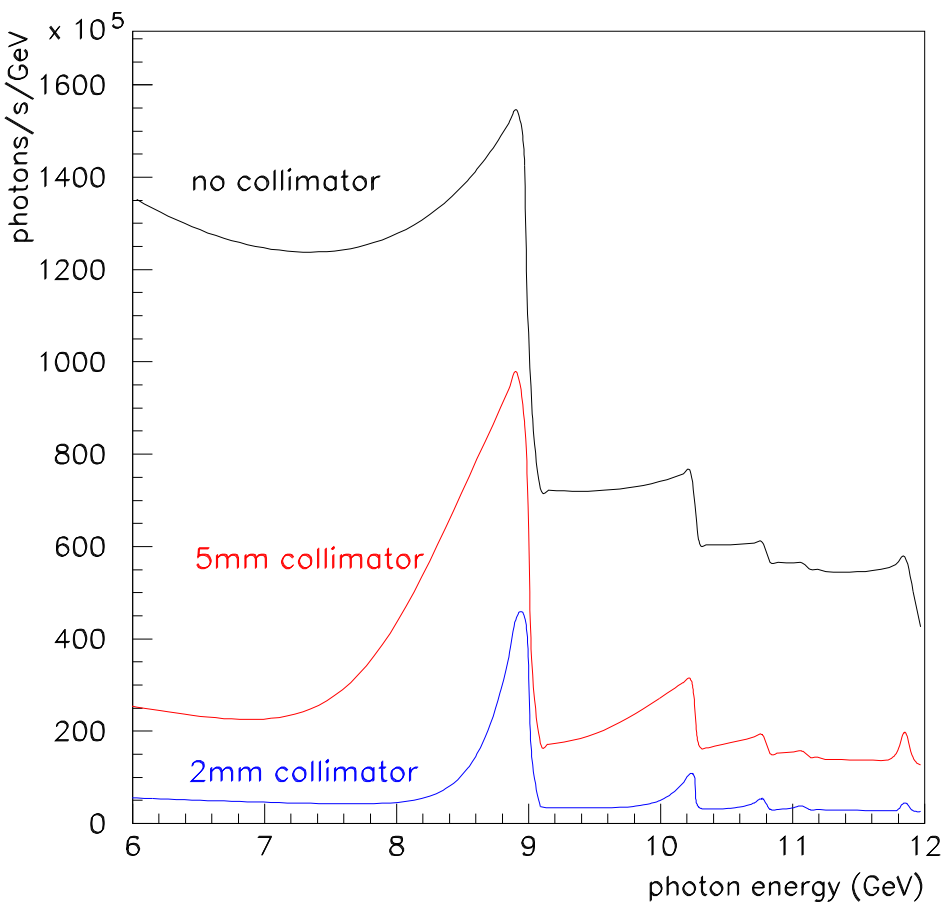

Figure 4.6: Coherent bremsstrahlung spectrum, calculated under the same conditions as in Fig. 4.5 , after collimation. The upper curve is the uncollimated spectrum from Fig. 4.5. The middle curve corresponds to a 5mm diameter collimator placed 80m downstream of the radiator, or approximately 0.75 m/E in collimator half-angle. The lower curve corresponds to a 2mm collimator in the same position, approximately 0.30 m/E

Second, note that the cut imposed on the coherent peak by collimation does not produce a perfectly sharp edge as would be expected from two-body kinematics. This is because a collimator cuts on radius at some fixed position which translates into a cut on emission angle only in an approximate way, and is why the curves in Fig. 4.6 are labeled by their collimator size and distance individually rather than their ratio which is the nominal collimation angle. Multiple scattering by the electron in the radiator prior to emission and beam spot size and divergence are the major contributors to the error involved in interpreting a collimator as a cut in emission angle. All of these effects have been incorporated into the analytical calculation of the yields from a collimated coherent bremsstrahlung source that has been used in preparing this report. Crystal imperfections, which amount to an intrinsic spread in the direction of the incoming virtual photon, are also accounted for in the calculation.

Third, note that the relatively weak collimation at $5\,mm$ reduces the incoherent background without significantly affecting the coherent flux near the maximum, and thereby almost doubling the polarization of the beam at the peak relative to the uncollimated case. Further reducing the collimator diameter continues to narrow the peak and reduce the incoherent flux relative to the peak, albeit at some cost in peak intensity. In the case of the $2\,mm$ collimator, the peak polarization is essentially that of the coherent component alone. For this collimator diameter most of the photon beam energy is being absorbed at the collimator. However the necessary flux in the collimated beam can be made up by increasing the electron beam current. provided there is adequate shielding around the collimator. The peak in Fig. 4.6 for a $2\,mm$ collimator contains 20M photons/s for an electron beam current of 1μA, which could be increased by a factor of up to 3 in the facility being planned for HALL D.

Fourth, note that the rate seen in the focal plane of the tagging spectrometer corresponds to the upper curve in Fig. 4.6, regardless of the collimation. This means that collimating the bremsstrahlung beam increases the rate in the tagger focal plane relative to what is seen at the detector. For example, running with the 2mm collimator and 10^7 photons/s in the main coherent peak implies according to Fig. 4.6 a rate of 70 MHz per GeV in the focal plane. Under these conditions, only a small part of the focal plane is in coincidence with the events of interest, which limits the rate of accidental tags to a reasonable level.

The net polarization of the beam under different collimation conditions is shown in Fig. 4.7. The dashed curves show how the maximum polarization in the peak varies as the peak energy is changed by rotating the crystal. The polarization in all cases is zero at the endpoint. Without collimation it rises as $(k-E)^2$, one power coming from the intensity of the coherent peak relative

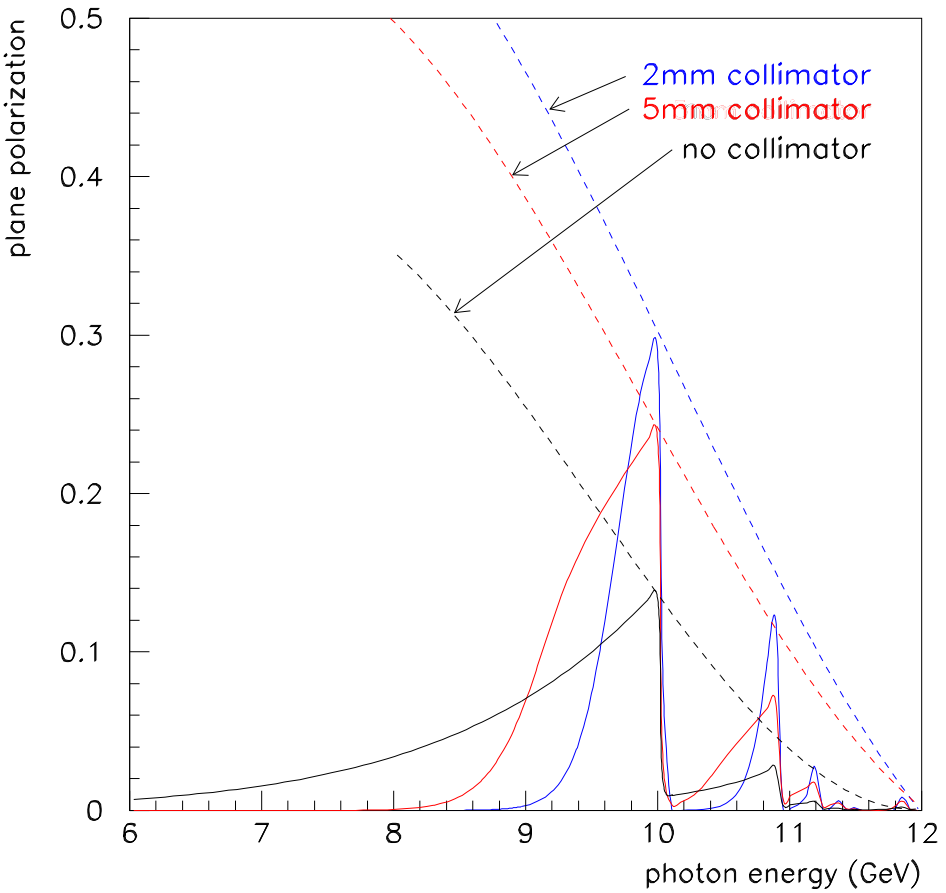

Figure 4.7: Plane polarization of the coherent bremsstrahlung beam, calculated under the same conditions as in Fig. 4.6. The dashed lines indicate the trajectory of the peak polarization as the peak energy is swept across the focal plane by rotating the crystal.

to the incoherent component going to zero linearly at the endpoint, and the other from the intrinsic polarization of the coherent photons also behaving like $(k - E)$ near the endpoint. Collimation allows one to essentially isolate the coherent component, so that the polarization available to the experiment rises from zero at the endpoint in a linear fashion. The dashed curves in Fig. 4.7 demonstrate this point.

In order to obtain the full polarization enhancement from collimation, it is necessary to have a distance between the radiator and collimator on the order of $100\,m$. This distance scale is set by the requirement that the collimator aperture must be large compared to the virtual electron beam spot on the collimator but small compared to the actual photon spot size. Fig. 4.8 shows the maximum polarization as a function of radiator-collimator distance for a coherent peak at 9 GeV. The collimator diameter is adjusted in this calculation to keep the collimation half-angle at 0.5 m/E. At zero distance the collimator has no effect except to attenuate the beam, and so the uncollimated polarization from coherent bremsstrahlung is obtained. At 100m separation distance the polarization enhancement has saturated. The design for HALL D calls for a radiator-collimator distance of $80\,m$.

4.2.3 Choice of radiator

The ideal radiator would be a layered structure with a strong transverse fields that alternate between layers spaced about $50\,nm$ apart, thus simulating the standing wave in a cavity driven by a 15 eV laser. While it is possible to construct ordered materials with unit cells as large as this, the self-shielding of atoms means that beyond the atomic length scale the residual fields are comparatively weak. Hence heterogeneous structures are not viable for use as a coherent radiator. Since the strong fields inside a solid are revealed at the atomic scale, the first requirement for a good radiator is that the unit cell be compact and closely packed. The best radiators are those with the smallest unit cells because these provide the best match between the atomic and the crystal form factors. This match is best for the light elements, and essentially prohibits the effectiveness of any materials heavier than carbon. An extensive survey of possible radiator materials is presented in Ref. [3]. In Table 4.1 is shown the figure of merit that those authors report for favored crystalline materials. The figure of merit is the product of the atomic times the crystal form factor evaluated at the leading peak, normalized to the value for diamond.

Table 4.1 shows that the list of viable materials for a crystal radiator is relatively short. Silicon would be an excellent choice from the point of view

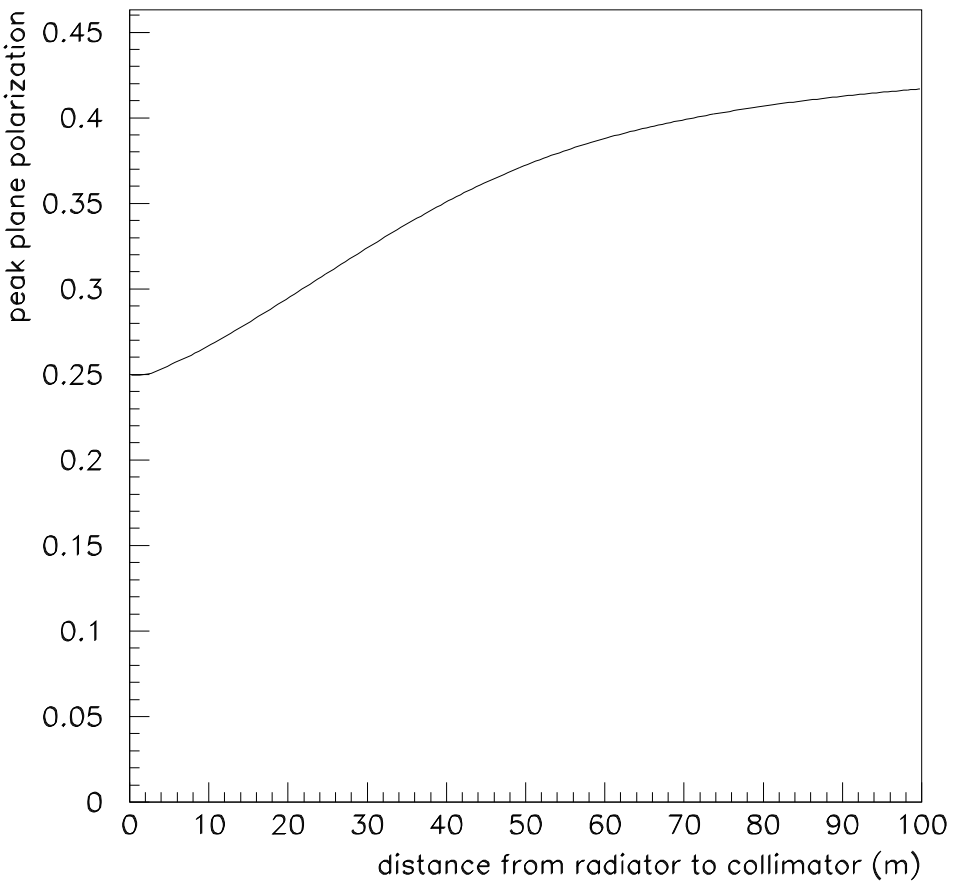

Figure 4.8: Maximum polarization *vs* radiator-collimator distance for a coherent peak at 9 GeV. The collimator diameter is varied in this calculation to keep the collimation half-angle at 0.5 m/E.

crystal	best reciprocal vector	$P/P_{diamond}$
diamond	2,-2,0	1.00
beryllium	0,0,2	0.86
boron	2,0,8	0.38
silicon	2,-2,0	0.19
Be_2C	2,2,0	1.10

Table 4.1: Figure of merit of various materials that might be used as a coherent bremsstrahlung radiator. This table is reproduced from Table 2 in H. Bilokon *et al.*

of price and fabrication, but unfortunately it is far inferior in terms of performance. Beryllium carbide is not a material that is familiar to the crystal growth industry, and nothing is known at present concerning its suitability for the growth of single crystals of large area. In general compound materials are more susceptible to radiation damage than are pure elements, which would argue in favor of diamond and beryllium metal. These two materials are comparable in terms of their performance.

Most of the experience to date with coherent bremsstrahlung has been with diamond radiators. Extensive expertise for handling large diamond crystals exists within the gem industry. High quality monocrystals of $6\,mm \times 6\,mm$ area were obtained by SLAC [2] some time ago from a jeweller, who was able to cleave a thin wafer from the face of a large high-quality gem. Those wafers that passed quality checks were then milled down to less than 100 μm using chemical erosion in an atomic oxygen discharge. Now three decades later, it is not clear whether this same route can be travelled again, as it owed its success in a large measure to a friendly contact within the gem business at that time. The cost of the entire gems from which the shavings were taken would have been prohibitive. Today other methods exist for growing single crystals which might be capable of producing diamonds of sufficient size and quality for this application. A variety of potential sources for single crystals are being pursued.

Beryllium is another material that might be used as a crystal radiator. Beryllium metal is widely used in industry, being preferred for its high strength-to-weight ratio and robustness, in addition to its transparency to X-rays. Thin films of high-purity beryllium are routinely produced for vacuum window applications, which use some of the same vacuum deposition techniques that

would be used for the growth of single crystals. As a radiator material, beryllium is distinguished as the metal with the highest Debye temperature, around 1400°K . The Debye temperature measures the temperature at which the thermal motion of the atoms in the lattice reaches the level of the zero-point motion due to their confinement in the lattice, as dictated by the uncertainty principle. A high Debye temperature indicates a stiff crystal lattice, in which the atoms have little liberty to move and so have large momentum fluctuations, as dictated by the uncertainty principle.

A high Debye temperature is important for a bremsstrahlung radiator material for three reasons. First, the cross section for coherent bremsstrahlung from a discrete crystal momentum vector $\vec{q}$ contains a factor $e^{-q^2/4M\theta_D}$ which reflects the fact that position fluctuations of atoms in the lattice diminish the coherent effect. This factor is near unity for the low-order crystal momenta provided that θ is sufficiently large. Second, the Debye temperature is, roughly speaking, a measure of the stability of the crystal structure and hence its readiness to form as a single crystal and to survive significant doses of radiation. Third, the radiator material will inevitably be heated by the beam, and will normally operate in vacuum well above the ambient temperature. A high Debye temperature means that there is a large range of temperatures over which the material may operate without degraded performance as a crystal radiator. The Debye temperature of diamond is about 2200° K. Past experience has shown that diamond meets all of the requirements for a good crystal radiator. There is good reason to believe that beryllium would function almost as well at substantially less cost, but this remains to be proved.

4.2.4 Crystal thickness

The range of permissible thicknesses for a crystal radiator is bounded both from above and below. It is bounded from above by multiple scattering of the electron beam as it passes through the radiator, which causes the divergence of the incident beam to grow, thereby enlarging the photon beam spot on the collimator face and degrading the degree to which collimation discriminates against the incoherent component in favor of the coherent part. It is bounded from below by the fact that the crystal must be of some minimum thickness in order to achieve the full coherent gain. In the calculation of the coherent bremsstrahlung process one begins by assuming an infinite crystal, although practically it is presumed to mean only that the crystal is large compared to the some characteristic scale. It is important to identify what the characteristic scale is in this problem in order to know how thin one can make the crystal without hurting performance. In the analogous case of the Mössbauer

effect, one can estimate the number of atoms participating in the collective absorption by looking at the emission time of the photon (lifetime of the radiating transition) and asking how many nuclei lie within the envelope of the photon wave packet. In the coherent bremsstrahlung process, the lifetime of the radiating system is given in the lab system by the uncertainty principle and by how far the electron energy deviates from its on-shell value between absorbing the virtual photon and emitting the real one. The latter quantity is almost exactly given by q_z , the virtual photon momentum component along the incident electron axis, which means that the electron travels a distance $\lambda = \hbar c/q_z$ during the interaction. For a given coherent peak at normalized energy x in the photon spectrum, the coherence length is given by

$$\lambda = \frac{2e(1-x)}{xm^2} \tag{4.3}$$

in units of $\hbar c$. From this simple argument one sees that the coherent gain goes linearly to zero at the endpoint, a result that is borne out by the full QED calculation. One also sees that the lower limit on crystal thickness imposed by the coherence length depends upon both the electron beam energy and the photon energy. For a 12 GeV beam energy and a 6 GeV coherent photon the coherence length is 18 nm, or about 50 unit cells for diamond. This shows that the coherence length does not impose a practical limit on how thin the radiator should be.

The effects of multiple scattering are best presented by showing the calculated spectra for various radiator thicknesses. In Fig. 4.9 is shown the photon spectrum for a 20 μm and a 100 μm radiator to demonstrate the effect. The 100 μm spectrum is scaled down by a factor of 5 to facilitate the comparison. The calculation assumed a 2 mm collimator located 80 m downstream of the radiator. The loss in normalized intensity with the thicker radiator, as well as the broadening of the left edge of the peak, is due to the enlarging of the photon beam spot on the collimator face from multiple scattering of the electron beam in the crystal prior to radiation. A 100 μm diamond crystal is roughly 10^{-3} radiation lengths thick. It is reasonable to run with as thick a radiator as is permitted by multiple scattering considerations, in order to keep the beam current to a minimum and prolong as much as possible the lifetime of the crystal.

4.2.5 Crystal mount

It has already been shown that in order to achieve appreciable coherent gain the crystal must be oriented so that the coherent peaks appear well below the

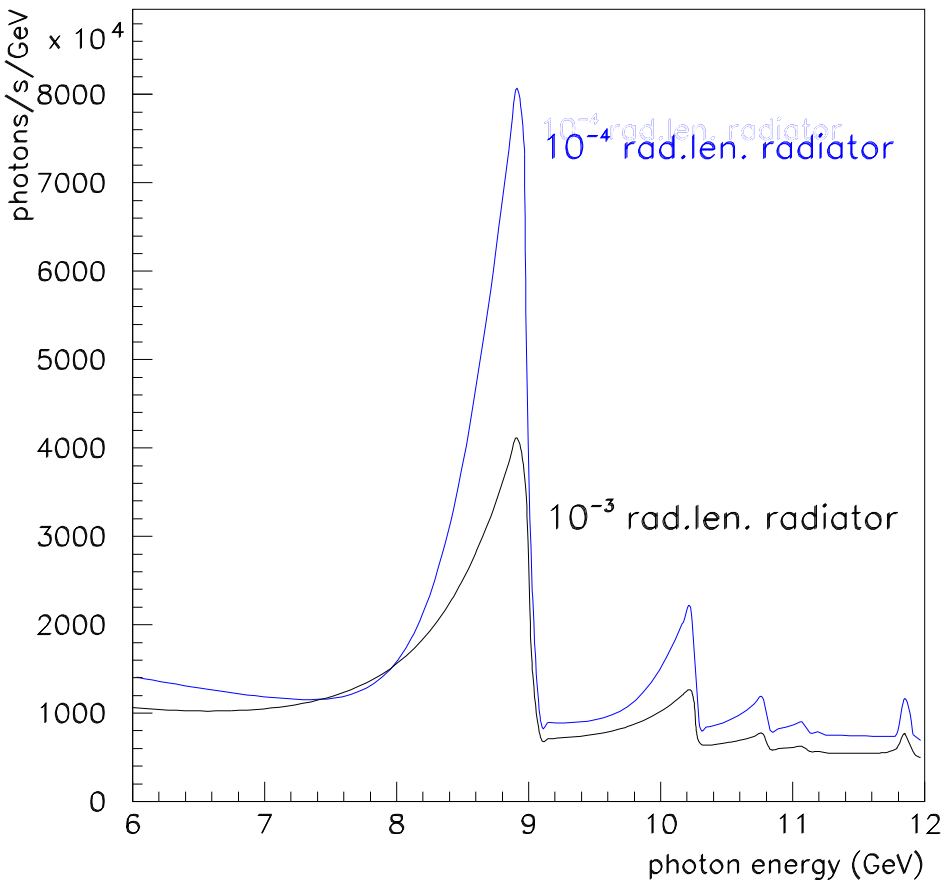

Figure 4.9: Collimated coherent bremsstrahlung spectrum from a 1μA electron beam at 12 GeV using diamond radiators of two different thicknesses. The calculation assumes a $2\,mm$ collimator located $80\,m$ from the radiator, and typical values for beam emittance and crystal quality.

end point. Eqn. 4.2 then implies that the orientation must be such that the crystal momentum dotted with the beam momentum be of order m^2 . Given a p of 12 GeV and q of $10keV$, this requires that the two vectors must be within 100μr of perpendicular to each other and that, within a range of angles of that order, the coherent peak sweeps out nearly the full range in x from 0 to 1. Hence both the incident beam angle and the angle of the crystal radiator must be stable at the level of a few μr in order to have a stable photon beam for running. At least one of the two must be adjustable in steps that are small compared to 100μr in order to have the ability to position the coherent peak at the desired energy. These requirements are most simply achieved using a precision two-axis goniometer. Commercial devices of this type exist with step sizes as small as required for this application. With two-axis remote control the crystal can be reoriented in a matter of minutes to produce a coherent beam of any desired energy and in either vertical or horizontal plane polarization modes.

Thermal effects in the crystal mount and small variations in the beam tune from the accelerator make long term stability and reproducibility more difficult to achieve than adequate controls for the initial setup. For this reason it is important that there be sufficient diagnostics present to monitor the crystal orientation relative to the beam. This diagnostic is provided by the rates in the tagger focal plane counters. From Fig. 4.5 it is clear that the critical angle between the beam and the crystal, as well as the quality of the crystal, are accurately reflected in the position and sharpness of the coherent edge in the focal plane rate profile. Better than simply monitoring the critical angle, the tagger profile provides a direct look at the photon beam spectrum prior to collimation. This means that there is no need for an absolute alignment of the crystal and goniometer to this level of precision, because only relative accuracy is required. The second angle is non critical, typically of order a degree, and does not need to be monitored. If conditions require it, a feedback system could be put in place to correct for drifts seen in the tagger focal plane profile by periodically adjusting the goniometer setting within predefined limits. This would involve a slow control system, and does not need to be designed in advance.

4.2.6 Crystal quality and lifetime

There are two considerations that fall under the heading of crystal quality. The first respects the quality of the original crystal, and the second is with regard to degradation from radiation damage. In the calculation of the coherent bremsstrahlung spectrum a perfect single crystal was assumed, but even the

very best crystals have some dislocations and other defects. Besides locally disrupting the regularity of the crystal, these defects impose stresses which produce small ripples in the crystal planes. If these ripples were amplified, the surface of a crystal would appear like a mosaic of planar regions with approximately parallel surfaces. The scale of deviations from planarity across the face of a single crystal is termed the *mosaic spread* of the crystal. The mosaic spread contributes in the same way as beam divergence to the smearing in the exact energy-angle relation for coherent photons.

The mosaic spread of a crystal can be measured by means of X-ray diffraction. At the time when the SLAC group was preparing their samples, a laboratory at the National Bureau of Standards had a state-of-the-art facility for these measurements. Their source of high-quality natural diamonds cleaved several samples and sent them to the NBS for rocking-curve measurements. Most of the crystals failed the tests, but among them were a few of sufficiently low mosaic spread to be acceptable. Ref. [2] does not report a value for the mosaic spread of the radiator, but from the sharpness of the coherent peaks in the beam spectra shown in the paper, one can infer that crystals with less than 50 μr mosaic spread were obtained in this way. Other coherent bremsstrahlung facilities that have operated at lower energy are less sensitive to mosaic spread because the characteristic angle scales like m/E. The calculations for this report assumed a mosaic spread of 50 μr for the crystal radiator.

The SLAC group found that the performance of their diamonds had degraded considerably after a total charge of 3 Coulombs had been accumulated over a surface of $6\,mm \times 6\,mm$ in area. They were able to recover a better performance for the damaged crystals by putting them through an annealing process. This translates to five weeks of running, or about two months of real time at 1μA of current, before the crystal would need to be removed for treatment. A small set of radiators of different thicknesses would accommodate a run plan that includes some running with maximum polarization, i.e. narrow collimation, a thin radiator and microamps of beam current, and running the rest of the time with a thicker radiator, less beam current and more modest collimation.

4.3 Electron Beam

The performance of the photon source is dependent upon the parameters of the electron beam in several important areas. The assumptions regarding the electron beam that were used in calculating the properties of the coherent bremsstrahlung source reported in this chapter are collected together in Ta-

energy	12 GeV
r.m.s. energy spread	< 10 MeV
transverse x emittance	10 $mm{\cdot}\mu$r
transverse y emittance	2.5 $mm{\cdot}\mu$r
electron polarization	longitudinal when available
minimum useful current	100 pA
maximum useful current	3 μA
x spot size at radiator	1.7 mm r.m.s.
y spot size at radiator	0.7 mm r.m.s.
x spot size at collimator	0.5 mm
y spot size at collimator	0.5 mm
position stability	± 200 μm

Table 4.2: Electron beam properties that were assumed in calculating the properties of the coherent bremsstrahlung source.

ble 4.2. Some of these parameters require further explanation. Only circular polarization can be transfered from the electron to the bremsstrahlung photon beam. In fact, helicity transfer from the electron is the only means available for generating photons with circular polarization in HALL D. Although circular polarization is less interesting than linear polarization from the point of view of meson photoproduction, having access to both kinds makes available a complete set of polarization observables. At the present a concrete design for the optics of the transfer beam line to HALL D does not exist, but when the design is made it would be useful to check that it can deliver circularly polarized photons to the hall.

4.3.1 Beam emittance requirements

The values for the electron beam emittances shown in Table 4.2 are estimates based upon the parameters of the current machine projected to 12 GeV. They were provided by V. Lebedev of the CEBAF accelerator division. The definition of emittance used here is the product of the r.m.s. widths of the beam in transverse position and divergence angle. Because synchrotron radiation occurs mainly in the horizontal plane inside the accelerator, the emittance values in x are generally larger than those for y.

The place where transverse emittance plays a critical role is at the photon collimator. For optimum effectiveness in collimation it is important that the electron beam spot at the collimator position be as small as possible. The

electron beam does not actually reach the photon collimator, being bent into the dump shortly after the radiator by the tagger magnet. But considering the optics of the electron beam as if the tagger dipole were switched off, the electron beam at the radiator can be projected forward $80\,m$ to form a virtual image on the collimator entrance plane. The position and size of this spot gives the the definition of the 0° emission angle for the photons. If this spot is small compared to the collimator aperture and is centered then the collimator does its job of removing photons with emission angle beyond the collimator half-angle. However, if the virtual spot is larger than the aperture then the collimator serves only to reduce the intensity of the beam and does not discriminate between coherent and incoherent beam components.

Note that this analysis does not place any specific limits on the size of the beam at the radiator. The beam spot can and should be larger there to avoid burning a hole in the radiator. For the SLAC coherent bremsstrahlung source the beam at the radiator was $6\,mm$ in diameter and focused to image a $2\,mm$ spot at the collimator positioned $91\,m$ downstream of the radiator. The focus ensures that photons emitted near zero degrees, even those far from the beam axis at the radiator, will pass near to the axis at the collimator position and so be seen at the experimental target. The virtual electron beam spot is not the same as the actual photon beam spot on the collimator, which is concentric with the former but larger. The collimator aperture is circular, so the choice was made to make the electron beam come to a virtual focus there with both x and y spot sizes equal there. This is why the beam spot on the radiator is asymmetric.

Figure 4.10 shows how the collimated photon spectrum depends upon the transverse emittance of the electron beam. To generate this plot the increases in emittance were simply translated into an increased virtual spot size on the collimator. This was done because it was assumed that the spot size of the electron beam on the radiator, already close to $2\,mm$ r.m.s., cannot be further inflated and stay contained within the limits of the crystal. When the virtual spot size becomes comparable with the collimator aperture then the collimation is rendered ineffective, and the photon spectrum and polarization revert to their uncollimated values. There is another connection between focal spot size and beam emittance that is connected with the requirement that all electrons enter the radiator at the same incidence angle with respect to the planes of the crystal. Practically, the divergence does not broaden the coherent peak provided that it is kept below the mosaic spread of the crystal. A conservative value for the allowable angular divergence δ in the electron beam at the radiator would then be 20μr . Taken together with a $500\ \mu m$ r.m.s. spot size at the focus, this leads to an emittance of $10\,mm{\cdot}\mu$r at $12\ GeV$.

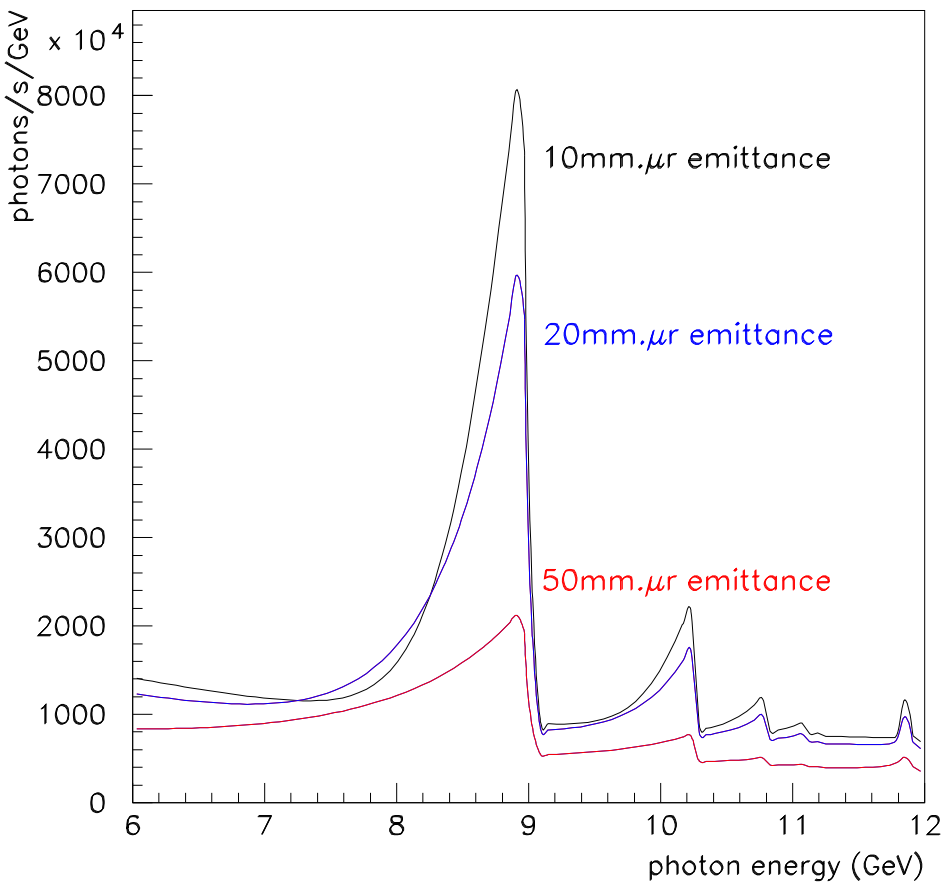

Figure 4.10: Coherent photon spectrum for three different values of the electron beam transverse emittance. The horizontal (shown on the plot) and vertical emittances are assumed to scale together. A $3.4\,mm$ collimator located $80\,m$ from the radiator was used for this calculation.

This corresponds to the upper curve in Fig. 4.10.

4.3.2 Electron beam line optics

Taking the electron beam out of the machine and focusing it onto a 500 μm spot requires some optics in the beam line leading up to the radiator. Translating the beam emittance into a r.m.s. values for the beam radius and divergence requires the knowledge of the β parameter, defined as the ratio of the r.m.s. beam size to its angular divergence. When it comes out of the accelerator, β is large, of order 1km, corresponding a very highly parallel beam. In order to focus a beam of emittance $10\,mm{\cdot}\mu$r down to a r.m.s. size of $500\mu r$, the β must be reduced from 1km down to 25 m by the use of focusing elements. The focusing must be done in both x and y axes separately to achieve the desired result, and must be accomplished by elements located along the transfer line from the accelerator vault to the surface. The focusing requirements are very specific for this type of source, and will require careful study in the design of the electron beam line.

Not only must the virtual electron spot be small enough to fit within the collimator aperture, but it must also be centered on the aperture and stable. In order to maintain a stable beam position on the collimator, the SLAC experiment [2] instrumented the collimator with a secondary-emission detector (SEQ). The detector was of the "pin-cushion" design and was installed as a segment of the collimator near the position of the shower maximum. The readout was divided into four quadrants, which read equal currents when the beam was properly aligned on the collimator. The SEQ was connected via a feedback loop to the last steering elements on the electron beam line prior to the radiator. From that distance a bend of only $10\mu r$ results in a shift of $1\,mm$ at the collimator position. Hence the beam alignment feedback system is effectively decoupled from the crystal orientation controls. Small deflections that are necessary to keep the beam centered on the collimator do not produce appreciable walk in the beam-crystal angle, and by using a goniometer to control the latter, the former can be operated in a feedback circuit that operates independent of the photon source energy controls. The experimental program in parity violation at Jefferson Lab has already designed a position stabilization circuit that is able to keep the beam position steady to within $20\mu m$ over a 20 m lever arm. A less sophisticated version of this circuit should be a part of the collimated photon source for HALL D.

4.3.3 Electron beam dump

The electron beam is dumped in the horizontal plane, as shown in figure 4.4. The horizontal bend offers several advantages over dumping the beam into the ground. The tagger magnet is easier to support if it sits in the horizontal position. It is also easier to mount and service the focal plane in this position. The dump itself is also more accessible in case it needs to be serviced. An above-ground dump also affords the possibility of running parasitic beam dump experiments that do not interfere with the operation of the experimental hall.

The primary design requirement for the electron beam dump is that it have a sufficiently high capacity to handle beams of the highest intensities foreseen for HALL D. A 60KW design would provide a a healthy margin for operation of a 12 GeV beam at 3μA and sufficient capacity to handle 3μA at 20 GeV in the case of a further upgrade.

4.4 Tagging Spectrometer

The HALL D tagging system will consist of a dipole magnet spectrometer with a set of plastic scintillation counters in the focal plane to tag photon energies between 50% and 95% of the incident electron energy.

4.4.1 Magnet

The tagging spectrometer magnet envisioned for HALL D is modeled closely on the existing tagger magnet in Hall B. Although the HALL D tagger will operate at a much higher energy, the combination of smaller deflection angle and smaller dynamic range (50% to 95% of the incident energy instead of 20% to 95%) result in a device which is comparable to the Hall B tagger in most of its dimensions, allowing the use of existing solutions to many engineering problems.

The tagger magnet will have a length of about 6.5 m and will deflect 12 GeV electrons along a path with radius of curvature 40 m, giving a deflection of about 9.4° (Fig. 4.11). If necessary, additional dipoles may be used downstream to guide the full-energy electron beam to the beam dump. The magnet gap width should be approximately 2.5 cm. A preliminary estimate of power requirements (using a coil configuration like that of the Hall B tagger) gives 500 amperes at 14 volts for 12 GeV operation.

The magnet poles themselves will form part of the vacuum system, and will be welded to a stainless steel vacuum chamber which terminates in a flange for mounting a thin exit window at the focal plane. The exit window, which

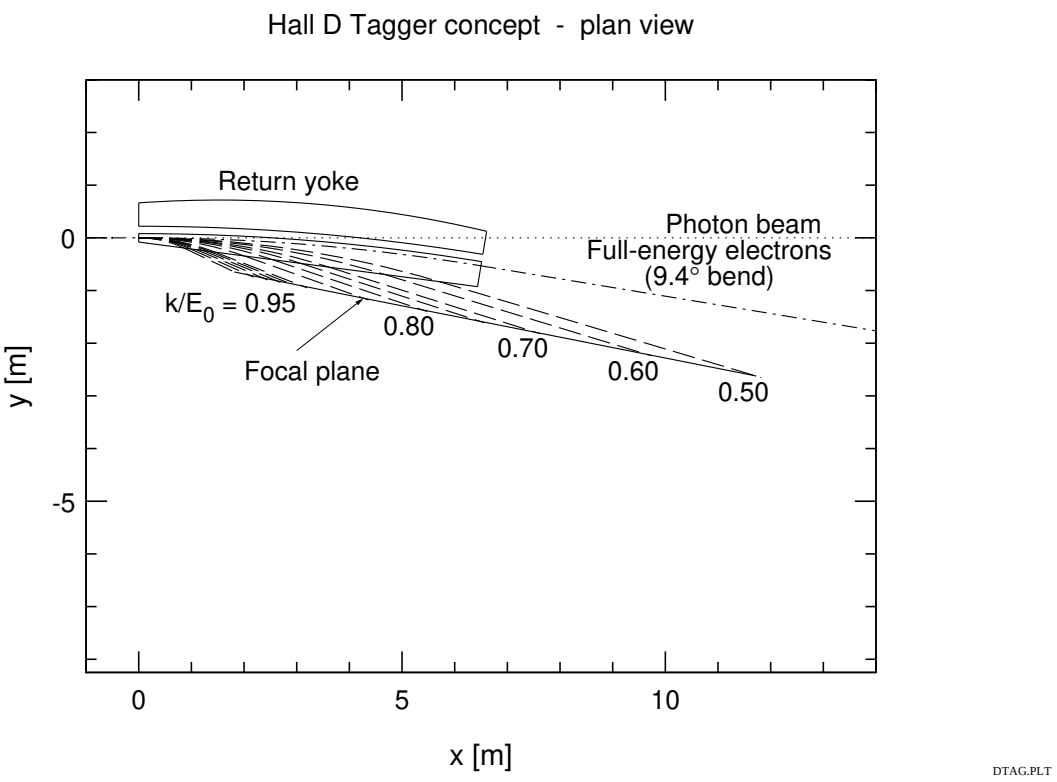

Figure 4.11: A plan view of the tagging spectrometer from above, showing the path of the primary beam and the trajectory of post-bremsstrahlung electrons of various recoil momenta.

must be about $10\,m$ long by $10\,cm$ wide, can be built in the same manner as the Hall B tagger window, using aluminized mylar backed by Kevlar cloth [6].

For the above dimensions, the magnetic field at 12 GeV is 1.0 Tesla. If the field is increased to about 1.7 Tesla (the point at which saturation effects become very large), the tagger can operate at a maximum beam energy of about 20.7 GeV. To assure adequate operation at a possible upgraded energy of 24 GeV, the dimensions and cost of the magnet would have to be scaled appropriately.

4.4.2 Spectrometer Optics

The bremsstrahlung electrons are deflected by angles varying from 25.4° to 16.6° over the range of tagged energies. For a radiator position located about $0.5\,m$ upstream of the magnet, a radial focus is obtained along a nearly linear focal surface. Some of the optical properties of the proposed spectrometer are summarized in Table 4.3.

Using the values in Table 4.3, one can calculate the attainable resolution of the tagging spectrometer, which is constrained by the following assumed electron beam sizes:

1. $\Delta p/p_0 = 0.8 \times 10^{-3}$ RMS
2. $\Delta x = 1.7\,mm$ RMS at radiator (horizontal)
3. $\Delta y = 0.7\,mm$ RMS at radiator (vertical)

The horizontal and vertical sizes at the radiator are different because of the different emittances and the need for a symmetric virtual focus at the collimator. For a horizontally-bending tagger magnet, the value x = $1.6\,mm$ would degrade the achievable energy resolution unless the electron beam is rotated to put the smaller emittance in the vertical direction. Table 4.4 indicates the effects of these values at the tagger focal plane, comparing them to the counter width required for an energy channel width of 0.2% E_0.

For a vertical bend, where $y = 0.7\,mm$ applies, the resolution is dominated by the 0.08% momentum width of the beam. If the tagger is built with a horizontal deflection, then the x resolution contribution for $k/E_0 < 0.7$ is comparable to the p contribution, unless the beam is rotated.

4.4.3 Focal-plane hodoscope

Since it is desired to run the experiments at high rate, the tagger detectors will not be incorporated into the trigger logic, but will instead be read out by high-

k/E_0	Bend (deg)	Drift (m)	Angle (deg)	$cm/\%E_0$ along FP	$cm/\%E_0$ perp.to ray	(x x)	(y y)	(y y') mm/mr
0.95	25.4	1.06	13.3	28.7	6.60	-0.81	3.42	5.8
0.90	21.2	1.78	9.8	24.7	4.19	-0.93	3.49	8.7
0.85	19.5	2.41	8.2	23.2	3.31	-0.97	3.46	11.2
0.80	18.5	3.00	7.3	22.4	2.85	-0.99	3.42	13.5
0.70	17.5	4.12	6.3	21.7	2.37	-1.01	3.34	18.0
0.60	16.9	5.21	5.7	21.3	2.13	-1.01	3.28	22.4
0.50	16.6	6.28	5.4	21.1	1.98	-1.06	3.24	26.2

Table 4.3: Optical parameters of the tagging spectrometer: Bend = deflection angle; Drift = distance from exit edge to focal plane; Angle = angle between electron path and focal plane; cm/$\%E_0$ = dispersion in units of cm per percent of the incident energy; (x x),(y y),(y y') = first-order transport matrix elements where x and y are radial and transverse coordinates respectively; the focal plane is defined by (x x')=0.

k/E_0	Width (mm)	p RMS (mm)	x RMS (mm)	y RMS (mm)
0.95	13.2	5.3	1.4	0.6
0.90	8.4	3.4	1.6	0.7
0.85	6.6	2.6	1.7	0.7
0.80	5.7	2.3	1.7	0.7
0.70	4.7	1.9	1.7	0.7
0.60	4.3	1.7	1.7	0.7
0.50	4.0	1.6	1.7	0.7

Table 4.4: Contributions to tagger energy resolution measured in units of length on the focal plane: Width = physical size of focal plane detector for $\Delta E = 0.002E_0$; p RMS = size due to energy spread of electron beam $p = .0008E_0$; x RMS = size due to horizontal spot size on the radiator $\sigma_x = 1.7\,mm$; y RMS = size due to vertical spot size on the radiator $\sigma_y = 0.7\,mm$.

resolution time-to-digital converters (TDCs) for off-line analysis. Assuming that the time correlation with the main detector can be done with a resolution of better than $3\,ns$, tagged photon rates of up to $100\,MHz$ can be utilized before accidental coincidences become a serious limit.

Electrons will be tagged in energy channels of width $0.002\ E_0$ ($25\ MeV$ at $E_0 = 12\ GeV$). This will result in an RMS energy resolution of about $0.001\ E_0$, which is consistent with the limits imposed by the beam as discussed in the previous section. As shown in Table 4.4, the width of a counter which defines such a channel varies from $13.2\,mm$ at $k/E_0 = 0.95$ to $4.0\,mm$ at $k/E_0 = 0.50$. The spacing of the counters along the focal plane will vary between 4.2 and $5.7\,cm$ according to the data of Table 4.3.

If each detector defines a single energy channel, some overlap with adjacent counters is desirable to avoid gaps in the acceptance and edge effects in the detectors. Because of the close tolerances involved in aligning such narrow counters for small fractional overlap, another solution would be to increase the energy width of the counters and align them so that adjacent counters overlap by 1/3 of their width. In this case, successive energy channels are defined by alternating coincidence and anticoincidence between adjacent counters. The principal disadvantage of this solution is that the counting rate in each scintillator is 3 times the value for the one-counter-per-channel design. For collimated coherent bremsstrahlung running, the coherent peak is confined to a very narrow energy region, especially when the photon energy is close to the endpoint. Under these conditions, individual counters may be required to sustain rates as high as $10\,MHz$, which will require special bases and electronics, and this rate will probably define the limiting rate for the experiments. Increasing the overlap of the counters would then require a reduction in the total event rate for coherent bremsstrahlung running, and thus is not an attractive solution.

The length of the counters (in the transverse direction) is determined by the desired efficiency for tagging uncollimated incoherent bremsstrahlung events near $k = 0.95E_0$. Counters of length $6\,cm$ will be more than 97% efficient at the endpoint of a $12\ GeV$ beam, and even more efficient at other photon energies. Since the time shifts within a $6\,cm$-long counter are less than $200\,ps$, excellent timing can be obtained using a single photomultiplier tube.

Thus the proposed configuration for tagging photons from 50% to 95% of the endpoint energy consists of 225 scintillation counters, each subtending an energy bin of about $0.002E_0$, with minimal (or no) overlap. The dimensions of each counter are approximately as follows: width = 4.0 to $13.2\,mm$, length = $60\,mm$, thickness $4\,mm$. Each counter is read out by a single high-rate photomultiplier tube, permitting rates up to $10\,MHz$ per counter. The counters are at least $4\,cm$ apart along the focal plane, so $2.5\,cm$ PMTs can be used without

alternating directions.

4.5 Operating Beam Intensity

Table 4.5 brings together the diverse set of parameters that must be considered in evaluating the optimum beam intensity at which an experiment using the coherent bremsstrahlung beam should operate. All four columns of numbers were obtained for the same beam conditions, except that the crystal orientation was adjusted to align the coherent intensity peak at the energy listed in row one. The second row labeled N_γ gives the integrated rate of beam photons in the coherent peak downstream of the collimator. Note the sharp decrease in the intensity of the coherent peak as the energy approaches the end point. By contrast, the incoherent bremsstrahlung flux is approximately constant over this range of energies. The third and fourth row show the height and width of the peak in the polarization spectrum of the beam. Rows four and five report the height and width of the peak in the tagging efficiency spectrum. The tagging efficiency is defined as the number of beam photons of a particular energy reaching the target divided by the corresponding rate in the tagging focal plane. Large tagging efficiencies are required in order to make effective use of tagging. The width of the peak in the tagging efficiency spectrum determines the width of the focal plane that would be active when running with collimation. The peak integral reported in row two is summed within the f.w.h.m. tagging efficiency window. Rows seven and eight give the photon beam power that is incident on the experimental target (and photon beam dump) and the photon collimator, respectively.

The last two rows in Table 4.5 give the inclusive and tagged rates for hadronic triggers from a $30\,cm$ liquid hydrogen target placed in the beam following the collimator. Note that the total hadronic rate is dominated by background (*i.e.* non-tagged) events associated with the low-energy component of the beam. This is why the total trigger rate is essentially constant while the flux in the coherent peak varies with peak energy over an order of magnitude. This table illustrates the value of having an electron beam energy well above the photon energy needed for the experiment.

E of peak	8 GeV	9 GeV	10 GeV	11 GeV
N_γ in peak	185 M/s	100 M/s	45 M/s	15 M/s
peak polarization	0.54	0.41	0.27	0.11
(f.w.h.m.)	(1140 MeV)	(900 MeV)	(600 MeV)	(240 MeV)
peak tagging efficiency	0.55	0.50	0.45	0.29
(f.w.h.m.)	(720 MeV)	(600 MeV)	(420 MeV)	(300 MeV)
power on collimator	5.3 W	4.7 W	4.2 W	3.8 W
power on target	810 mW	690 mW	600 mW	540 mW
total hadronic rate	385 K/s	365 K/s	350 K/s	345 K/s
tagged hadronic rate	26 K/s	14 K/s	6.3 K/s	2.1 K/s

Table 4.5: Operating parameters for an experiment using the coherent bremsstrahlung beam. The calculation assumes a 12 GeV electron beam energy and a 3.4 mm collimator 80 m downstream from a radiator of thickness 10^{-4} radiation lengths. The electron beam current is taken to be 3μA. The rates in the detector (last two rows) are calculated for a 30 cm hydrogen target and an open hadronic trigger.

List of Figures

4.1 Generic diagrams for hard photon production. 3
4.2 Photon energy spectrum from the Compton back-scatter source 5
4.3 Photon power spectrum from an oriented diamond radiator. . 8
4.4 Schematic plan view of the photon beam line 10
4.5 Coherent bremsstrahlung spectrum 13
4.6 Coherent bremsstrahlung spectrum after collimation. 15
4.7 Plane polarization of the coherent bremsstrahlung beam . . . 17
4.8 Maximum polarization *vs* radiator-collimator distance. . . . 19
4.9 Collimated coherent bremsstrahlung spectrum 23
4.10 Coherent photon spectrum for three different values of the electron beam transverse emittance. 28
4.11 A plan view of the tagging spectrometer 31

List of Tables

4.1 Figure of merit of various materials that might be used as a coherent bremsstrahlung radiator. 20
4.2 Assumed electron beam properties 26
4.3 Optical parameters of the tagging spectrometer. 33
4.4 Contributions to tagger energy resolution. 33
4.5 Operating parameters for an experiment using the coherent bremsstrahlung beam. 36

Bibliography

[1] C. Keppel. Development of a Compton-backscattered photon source for Hall B at Jefferson Lab. In *Physics with 8+ GeV Photons Workshop.* Workshop in Bloomington IN, July 14-16 1997, proceedings available from Jefferson lab.

[2] W. Kaune, G. Miller, W. Oliver, R.W. Williams, and K.K. Young. Inclusive cross sections for pion and proton production by photons using collimated coherent bremsstrahlung. *Phys. Rev.*, D **11**(3):478–494.

[3] H. Bilokon, G. Bologna, F. Celani, B. D'Ettorre Piazzoli, R. Falcioni, G. Mannocchi, and P. Picchi. Coherent bremsstrahlung in crystals as a tool for producing high energy photon beams to be used in photoproduction experiments at CERN SPS. *Nuclear Inst. and Meth.*, **204**:299–310.

[4] G. Diambrini-Palazzi. *Revs. Mod. Phys.*, **40**:611, 1968.

[5] U. Timm. *Fortschr. Phys.*, **17**:765, 1969.

[6] S.K. Matthews *et al. Nuclear Inst. and Meth.*, **A 421**:23, 1999.